International Journal of Non-Linear Mechanics 147 (2022) 104194

Contents lists available at ScienceDirect

International Journal of Non-Linear Mechanics

journal homepage: www.elsevier.com/locate/nlm

Low-to-high frequency targeted energy transfer using a nonlinear energy sink with softening-hardening nonlinearity

Chengen Wang, Ethan J. Krings, Anna T. Allen, Eric J. Markvicka, Keegan J. Moore *

Department of Mechanical and Materials Engineering, University of Nebraska-Lincoln, Lincoln, NE 68588, United States of America

ARTICLE INFO

Keywords:
Softening–hardening
Nonlinear energy sink
Targeted energy transfer
Nonlinear vibration

ABSTRACT

This paper investigates the performance of a nonlinear energy sink (NES) equipped with a softening–hardening (SH) element for mitigating vibrations that occur below its linear, low-energy frequency. First, an SH elastic struct is constructed, tested quasi-statically, and the resulting restoring force is modeled using a polynomial. Next, the SH polynomial is non-dimensionalized and a theoretical system composed of a linear oscillator (LO) and NES is studied where the NES has a linear, low-energy frequency above that of the LO. The underlying nonlinear normal modes (NNMs) of the system are studied by using harmonic excitation and tracking the changes in the frequency response functions. The transient performance of the NES is investigated and compared with that of a NES with the same linear stiffness but only a cubic nonlinearity. The theoretical performance of the NES is verified using a comparable experimental system that incorporates the SH elastic struct built in the beginning of the paper. The results of this work demonstrate that an SH NES is capable of mitigating vibrations that occur at frequencies below its own linear, low-energy frequency.

1. Introduction

Nonlinearity is present in nearly all structures, and this nonlinearity causes the dynamics of the system to change based on the energy stored in the system. Specifically, the frequencies and mode shapes governing the motion of the structure change as the energy in the system varies. In this sense, the system can be said to possess nonlinear normal modes (NNMs) [1,2], which are time-periodic oscillations that are not necessarily synchronous and represents a nonlinear extension of linear normal modes. This distinction makes nonlinear systems more complicated than their linear counterparts [3] and introduces phenomena, such as internal resonances, that do not arise under linear vibrations.

One of the most prolific implementations of nonlinearity is the phenomena of targeted energy transfer (TET), which involves the irreversible transfer of energy from a primary linear structure to a series of local, nonlinear attachments called nonlinear energy sinks (NESs) [4–6]. However, in the typical application of TET, the NES is equipped with a strong hardening nonlinearity and, thus, must have a linear (low energy) frequency that is less than that of the mode of the primary linear structure that it is intended to absorb energy from [3,7,8]. In other words, if the linear frequency of the NES is above that of a mode in the primary structure, then the NES will not be able to dissipate energy in that mode and, instead, acts as a mass effect and lowers that mode's natural frequency. This behavior can be seen in [9] where an NES installed on a model airplane wing was tuned to interact with the second mode of the wing and, thus, was unable to mitigate the response of the first mode. Moreover, the design of nonlinearities in real NESs often result in a weak linear stiffness, such that the NES has a non-zero frequency and lowering that linear frequency often comes with sacrificing the strength of the nonlinearity. In the case of highly flexible structures that possess multiple modes at low frequencies (below 10 Hz), an NES with even a weak linear stiffness may be unable to mitigate the motion of the lowest flexible modes.

To overcome this limitation, many efforts have been accomplished, one of which is applying quasi-zero stiffness (QZS) to achieve passive energy isolation in low dynamic regime [10–13]. In this context, QZS can be obtained by combining a positive stiffness component with a negative stiffness adjustment, resulting in a combination of linear, plateau, and hardening segments as seen in Fig. 1. In practice, QZS isolators can be achieved in many mechanisms: cam-roller [14–16], buckled beams [17–20] and many other structures [21–25]. By applying QZS, a softening–hardening (SH) process is introduced to the NNMs of the system, which will enable the NES to interact with and mitigate the modes of the primary structure that have frequencies below the linear, low-energy frequency of the attachment.

In this work, we posit that an NES with an SH spring will be able to interact with and mitigate vibrations that occur at a lower frequency than the linear frequency of the NES. The reason is that the transition into and the plateau region of the SH spring produces a softening effect that reduces the frequency of the NES. The reduction in frequency allows the NES to interact with modes that have linear frequencies

* Corresponding author.
E-mail address: kmoore@unl.edu (K.J. Moore).

https://doi.org/10.1016/j.ijnonlinmec.2022.104194
Received 17 April 2022; Received in revised form 5 August 2022; Accepted 13 August 2022
Available online 24 August 2022

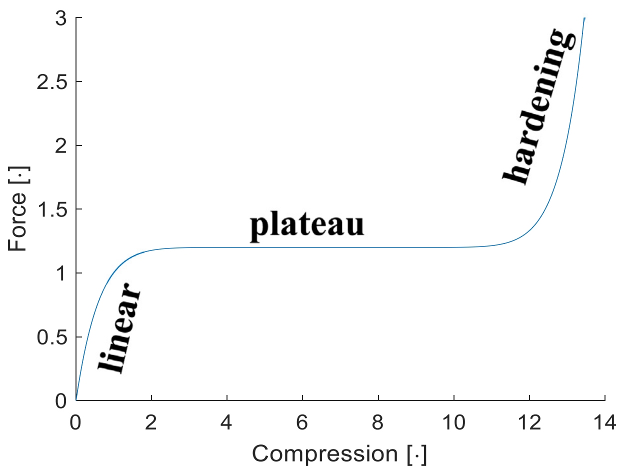

Fig. 1. A typical compression plot of a softening–hardening (SH) process, and it is composed of 3 parts: a linear, plateau, and stiffening part.

below that of the NES's linear frequency. Next, we aim to evaluate this hypothesis computationally and experimentally as well as the performance of an SH NES with a linear frequency below the targeted mode for mitigation. The paper is organized as follows. Section 2 presents a design of the SH spring based on an elastic strut element proposed by Bunyan and Tawfick [26] followed by the experimental characterization and modeling of its restoring force. Section 3 presents a computational study into the effectiveness of an NES equipped with an SH spring at mitigating the motion of a linear oscillator (LO), and comparisons are made with a comparable NES with only a cubic stiffness nonlinearity. Section 4 presents the experimental validation of the computational results for the NES with SH spring. Finally, Section 5 presents concluding remarks about this work.

2. Design, identification, and nondimensionalization of softening–hardening element

2.1. Elastic strut elements

In this work, we consider the elastic strut elements created by Bunyan and Tawfick [26] as shown in Fig. 2, which consists of a triangular shaped strut that undergoes buckling when compressed. The elastic strut elements were designed using Autodesk Inventor Professional and include two bolt holes for clamping onto structures. The CAD model is shown in Fig. 2(a). The strut has a width of 0.0221 m, a height of 0.0193 m, and a thickness of 0.00483 m. The arms have widths of 0.00178 m and is chosen based on the design described by Bunyan and Tawfick [26]. A dimensioned drawing of the elastic strut is provided as supplementary material.

To manufacture the springs, master patterns of the spring were created with an SLA 3D printer (Form 3, Formlabs Inc). The masters were coated with a mold release spray (Universal Mold Release, Smooth-On Inc) to prevent adhesion of silicone to the masters during the next step. A duplication silicone (Elite Double 32, Zhermack) was then cast around the master patterns to create negative molds of the spring geometry. The master patterns were removed from the silicone negatives after the silicone was set. To create the springs, a urethane rubber was prepared by combining part A to B at a 1:1 mass ratio and then mixing in a planetary mixer for 2 min (SpeedMixer DAC 400.2 VAC, FlackTek Inc). Mold release spray was applied to the silicone negatives to prevent the rubber from adhering to the molds. The uncured rubber was then cast into the silicone negatives and cured under 40 psig of pressure at room temperature for 24 h. Fig. 2(b) demonstrates the completed spring element.

Table 1
Parameters of the polynomial model for the SH elastic strut element with dimensional and nondimensional values.

Parameter	Dimensional values	Dimensionless values
a_1	4918 N/m	0.6271
a_2	-4.723×10^6 N/m^2	−1
a_3	1.847×10^9 N/m^3	0.6494
a_4	-3.055×10^{11} N/m^4	−0.1784
a_5	1.903×10^{13} N/m^5	0.0184

Table 2
R-squared values for the seven different polynomial models computed using the 1 mm/min measurement.

Order	3	4	5	6	7	8	9
R^2 value	0.9756	0.9838	0.9907	0.9909	0.991	0.9912	0.9912

2.2. Measurement and identification of strut element restoring force

The compressive behavior of each element was then characterized through a series of compression tests using a universal testing machine (Instron 5966) with a 200 N load cell. To aid in the testing, a plastic mount was 3D printed and installed in the Instron machine's grip to provide a smooth surface for compressing the strut. The mount is shown in Fig. 3(a). The compression tests consisted of 5 pre-cycle compression tests to eliminate any initial hysteresis of the material and 3 formal cycles with an 8 mm maximum displacement. The compression tests were completed for testing speeds of 10 mm/min, 5 mm/min, and 1 mm/min and the resulting restoring forces are depicted in Fig. 4.

As shown in Fig. 4, the restoring force is observed to be similar for all three testing speeds and there is minimal hysteresis between the loading and unloading curve. As such, the spring can be approximated as elastic and only one of the three speeds is needed to identify a model for the restoring force. To this end, we use the third cycle from the 1 mm/min loading speed to fit a fifth-order polynomial to the restoring force in the following form:

$$F(x) = \left(a_1 |x| + a_2 |x|^2 + a_3 |x|^3 + a_4 |x|^4 + a_5 |x|^5\right) \operatorname{sgn}(x). \quad (1)$$

This model is chosen because it provides a symmetric restoring force under both compression and tension, and a symmetric restoring force will be used in the theoretical study and in the experimental system. The parameters were identified using the Curve Fitting toolbox in MATLAB® and the dimensional values are provided in Table 1. The model restoring force is plotted on top of the measured force and the resulting R-squared value is 0.9907 between the model and the experiment (Fig. 4(b)). We determined that the fifth-order model was optimal by fitting third-order through ninth-order polynomials using the same procedure as the fifth-order, which revealed that the fifth-order was the lowest order where a considerable increase in R-squared value occurred. The R-squared values for all of the polynomial models are provided in Table 2. Note that, during the compression test of the elastic strut, hysteresis can be observed from the difference between the compression and the relaxation loops. However, viscoelastic effects were not observed as the behavior of the springs is nearly identical for all speeds and, thus, these effects are neglected as secondary.

3. Theoretical study

3.1. System model and nondimensionalization

We consider the dynamics of a linear oscillator (LO) with a nonlinear energy sink (NES) installed on it. The LO is linearly coupled to the ground whereas the NES is nonlinearly coupled to the LO using the SH element (i.e., the polynomial model in Eq. (1)). The system is depicted in Fig. 5 and the governing equations of motion are

$$m_1 \ddot{x} + d_g \dot{x} - d_c \dot{\delta} + k_g x - \sum_{n=1}^{5} a_n |\delta|^n \operatorname{sgn}(\delta) = 0, \quad (2)$$

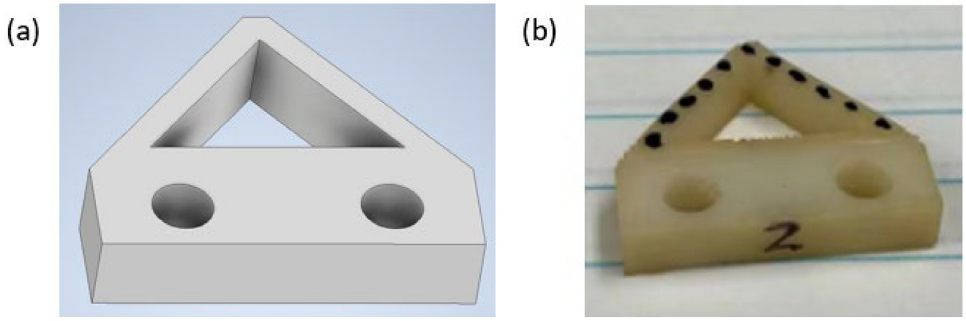

Fig. 2. (a) CAD model of the elastic strut elements and (b) the corresponding experimental part.

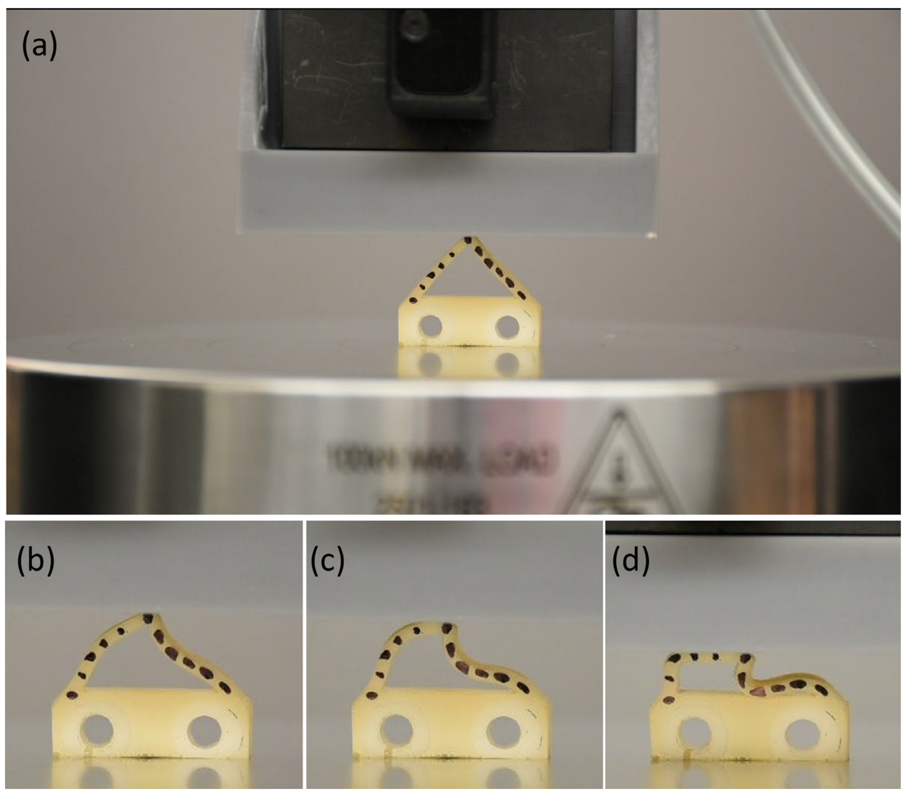

Fig. 3. (a) Configuration of the compression test on Instron machine with the 3D-printed mount and photographs of the (b) linear phase, (c) plateau (softening) phase, and (d) stiffening phase of the elastic strut element.

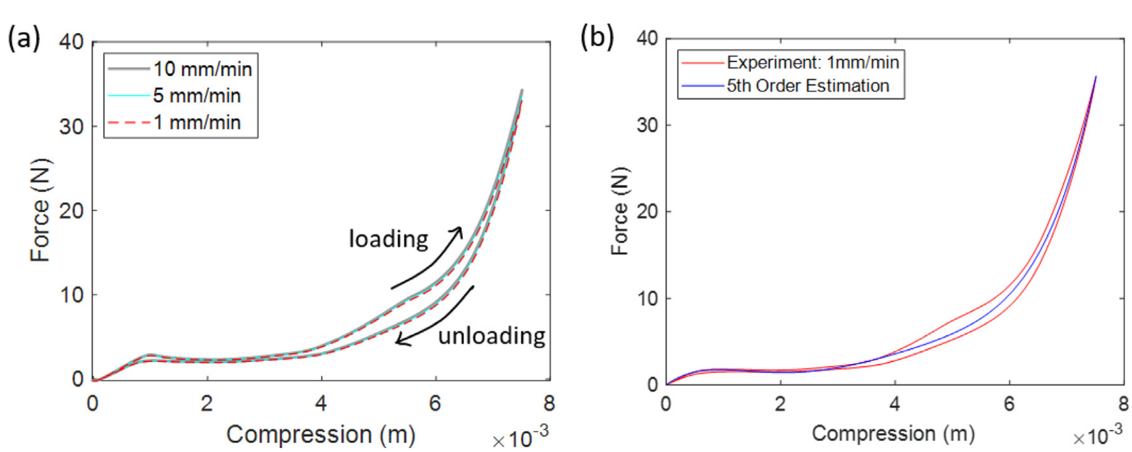

Fig. 4. (a) Compression curve of the elastic strut elements under testing speeds of 10, 5 and 1 mm/min. (b) Curve fitting of the compression curve of the elastic strut elements. Red line: experimental compression curve (1 mm/min); blue line: fitting curve of the compression curve using 5th order polynomial.. (For interpretation of the references to color in this figure legend, the reader is referred to the web version of this article.)

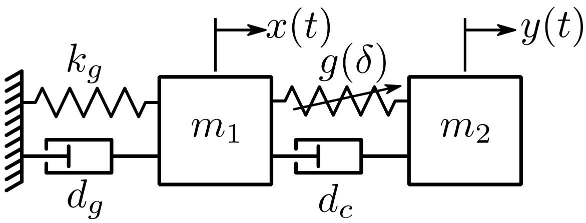

Fig. 5. Schematic of the two degree-of-freedom system considered here where the two oscillators are coupled using an SH spring or a polynomial, where $g(\delta) = \sum_{n=1}^{5} a_n |\delta|^n \operatorname{sgn}(\delta)$ and $\delta(t) = y(t) - x(t)$.

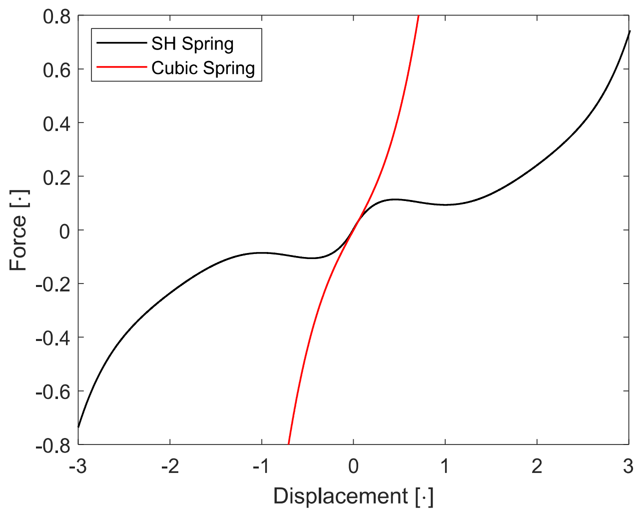

Fig. 6. Dimensionless compression curve of the SH spring and the cubic spring.

$$m_2\ddot{y} + d_c\dot{\delta} + \sum_{n=1}^{5} a_n |\delta|^n \operatorname{sgn}(\delta) = 0, \tag{3}$$

where $\delta(t) = y(t) - x(t)$. The equations of motion are nondimensionalized into the following forms

$$\ddot{\xi}_1 + \lambda_g\dot{\xi}_1 - \lambda_c\dot{\rho} + \xi_1 - \sum_{n=1}^{5} \beta_n |\rho|^n \operatorname{sgn}(\rho) = 0, \tag{4}$$

$$\varepsilon\ddot{\xi}_2 + \lambda_c\dot{\rho} + \sum_{n=1}^{5} \beta_n |\rho|^n \operatorname{sgn}(\rho) = 0, \tag{5}$$

where $\rho(t) = \xi_2(t) - \xi_1(t)$. The resulting parameters are related to the original dimensional parameters through the following relations

$$\varepsilon = \frac{m_1}{m_2}, \lambda_g = \frac{d_g}{\sqrt{m_1 k_g}}, \lambda_c = \frac{d_c}{\sqrt{m_1 k_g}}, \tag{6}$$

and the SH spring parameters are given by

$$\beta_1 = \frac{a_1}{k_g}, \beta_2 = \frac{a_2}{\sqrt{k_g a_3}}, \beta_3 = \frac{a_3}{a_3}, \beta_4 = a_4\sqrt{\frac{k_g}{a_3^3}}, \text{and } \beta_5 = \frac{a_5 k_g}{a_3^2}. \tag{7}$$

The dimensionless parameters for the SH spring are provided in Table 1 and the restoring force is plotted in Fig. 6 along with the restoring force of System II discussed in the next subsection.

3.2. Parameter selection

As stated previously, we hypothesize that an SH NES could mitigate vibrations that occur at frequencies below its linear frequency. We consider two versions of the same system: System I incorporates the SH spring element using the parameters listed in Table 1 and System II includes only a cubic stiffness nonlinearity. Specifically, the equation of motion governing the NES in System II is

$$\varepsilon\ddot{\xi}_2 + \lambda_c\dot{\rho} + \beta_1\rho + \rho^3 = 0. \tag{8}$$

Table 3
Non-dimensional parameters of the two systems considered.

Parameter	System I	System II
LO Mass	1	1
ε	0.1	0.1
λ_g	0.02	0.02
λ_c	0.02	0.02
β_1	0.6271	0.6271
β_2	−1.241	0
β_3	1	1
β_4	−0.3408	0
β_5	0.0438	0

Note that in both systems, the NES has a linear frequency higher than that associated with the LO. The nondimensional parameters of each system are provided in Table 3. Among these parameters, those governing the LO are selected based on typical nondimensional values in previous studies [27,28]. Note that, the coupling damper, λ_c, is assumed to be equal to the grounding damper, λ_g, because the SH element is made from polyurethane and is expected to introduce large damping compared to a metallic component (e.g., wires undergoing large deformations).

3.3. Nonlinear normal mode study

To build an understanding for the dynamics of this system, we consider the NNMs that govern the frequency transitions that arise due to the nonlinearity. Based on the definition provided earlier, one approach to investigating the NNMs is to plot how the frequency-response functions (FRFs) change as the amplitude or energy of the system is varied [1,29–34]. To this end, we consider the response of the system under harmonic excitation, in the form $F(t) = P\sin\omega t$, applied to directly to the LO with zero initial conditions for a total non-dimensional time of 5000 with a step size of 2e–2. We considered 500 different forcing amplitudes logarithmically spaced from 10^{-4} to 10^2 and 501 different frequencies linearly spaced from 0.1 to 10. For each simulation, we compute the FRFs by dividing the maximum displacement of the LO and NES in the time window [4800, 5000] by the input force P. This window is chosen to ensure that the transient response has fully died out and that the maximum displacement is due to the harmonic forcing only. We choose the maximum displacement because the response may not exhibit a steady-state amplitude or even a periodic response when internal resonances are activated in the dynamics. Nevertheless, this approach provides a good window into how the frequency behavior of the system evolves as the amplitude (energy) increases.

We depict the resulting FRFs for the LO, NES, and the relative displacement in Fig. 7 with the receptance shown as a colormap with darker colors representing low receptance and lighter colors representing high receptance. At low forcing amplitudes (below 0.1), the response of the system is governed by two nearly linear modes of vibrations as shown by the two horizontal bands of high receptance. In this case, the low-frequency band represents the first NNM and corresponds to in-phase motion of both masses at a frequency of 0.94 with the NES moving nearly the same amount as the LO (the corresponding linear, mass-orthonormalized mode shape is given by [0.938, 1.095] with the first and second entries corresponding to the LO and NES amplitude, respectively). The high-frequency band represents the second NNM and corresponds to out-of-phase motion of the two masses at a frequency of 2.64, such that the second NNM has a low-energy, linear frequency 2.81 times that of the first NNM. Note that, unlike typical NESs with negligible linear stiffness, the installation of the NES on the LO introduces the second NNM into the dynamics of the system and this is confirmed by the fact that the response is dominated by motion in the NES at frequencies around the second NNM. Moreover, the corresponding mass-orthonormalized mode shape

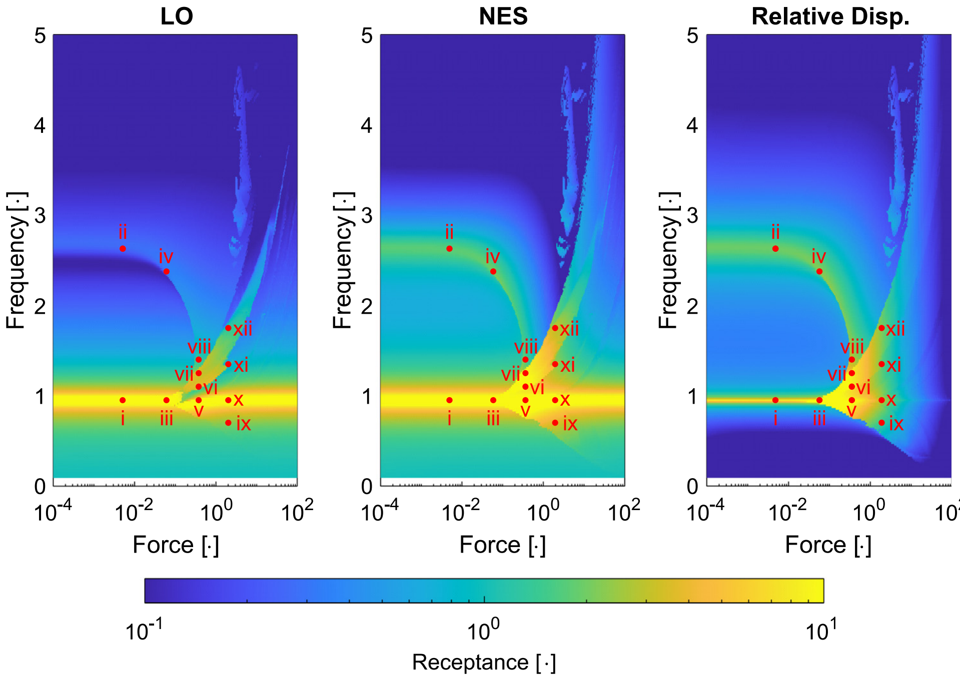

Fig. 7. FRF of steady state response of System I under harmonic excitation with varying forcing amplitude and frequency.. (For interpretation of the references to color in this figure legend, the reader is referred to the web version of this article.)

Table 4
Forcing frequency and amplitude combinations chosen to demonstrate the different behaviors of the theoretical system with SH element.

Point	Frequency, ω	Force, P	Point	Frequency, ω	Force, P
i	0.95	0.005	vii	1.25	0.372
ii	2.63	0.005	viii	1.4	0.372
iii	0.95	0.06	ix	0.7	2
iv	2.377	0.06	x	0.95	2
v	0.95	0.372	xi	1.35	2
vi	1.1	0.372	xii	1.75	2

for the corresponding linear second mode is [−0.346, 2.967], such that the motion of the NES more than 8.5 times that of the LO when the second mode is excited. Above a force of 0.01, the second NNM decreases in frequency until it appears to intersect the first NNM. The decrease in frequency is due to the buckling of the spring that results in a softening-type nonlinearity. The intersection occurs at a forcing amplitude of approximately 0.3 and after this force, the frequency of the second NNM increases away from that of the first NNM.

The decrease and subsequent increase in frequency of the second NNM leads to the possibility of internal resonances where energy is pumped from the first NNM into the second NNM. The result of such internal resonances is the presence of strongly modulated responses (SMRs) [3] where the LO and NES exhibit strong beating behavior when forced harmonically. When excited impulsively, the internal resonances would cause the motion of the LO to rapidly decay resulting in a dramatic reduction in its settling times. To investigate potential internal resonances, we selected twelve combinations of forcing amplitude and frequency as shown on the FRFs in Fig. 7, and present the corresponding displacements of the LO and NES in Fig. 8. Note that the time axis on each plot in Fig. 8 has been chosen to capture the behavior clearly on an individual basis. The forcing frequency and amplitude combinations are reported in Table 4.

The first two points (i and ii) depict the approximately linear response of the first and second NNMs, respectively, with point i showing in-phase motion and point ii showing out-of-phase motion. Point iii corresponds to a SMR indicating that the LO and NES are interacting with each other through internal resonances, such that we can observe interactions arising for weak forcing ($P = 0.06$) at the linear frequency of the first NNM ($\omega = 0.95$). Point iv depicts out-of-phase motion similar to the motion of point ii, which implies that the internal resonances are facilitated by the first NNM at this forcing level. Looking at point v, which is at the same frequency as point iv but at a magnitude of forcing higher, we find that the motion has returned to a simple in-phase motion as observed in point i. In fact, the response in point v is nearly identical to that in point iv except for the difference in amplitude and a slight difference in phase. Points vi and vii exhibit SMR similar to point iii indicating that the LO is transferring energy into the NES through internal resonances. Point viii exhibits nearly out-of-phase motion, which indicates that this point lies on a non-interacting branch of the second NNM whereas points vi and vii lie on interacting parts of the branch. Point ix depicts in-phase motion with the NES moving more than the LO, such that the portion of the FRF that fans downwards for $P > 1$ corresponds to in-phase motion with no nonlinear interactions between the LO and NES. Point x shows in-phase motion with the LO and NES having nearly the same amplitude, which indicates that the bright horizontal band now exhibits nearly linear motion. Finally, points xi and xii depict quasi-periodic or aperiodic motions indicating that the system responds chaotically within the band of increasing frequency of the second NNM.

3.4. Transient performance of SH NES

To investigate the performance of the SH NES, we consider the response of the system under the initial conditions $\xi_1(0) = \xi_2(0) = \dot{\xi}_2(0) = 0$ and $\dot{\xi}_1(0) = v_0$, such that an initial velocity is applied to only the LO, which is equivalent to exciting the LO using an impulsive force. We simulated the response of the system for 1000 logarithmically spaced initial velocities for the range $v_0 \in [10^{-3}, 10^3]$, which provides a large enough range to probe the entire dynamics of the system. The response was simulated using *ode45* in MATLAB® for a time step of 0.01 for a total time of 3000. Additionally, the relative and absolute tolerances of the solver were both set to 10^{-12}. This combination of parameters ensures that the system can be integrated accurately at high initial velocities. We consider two different metrics for assessing the performance of the SH NES: first, we compare the percent energy

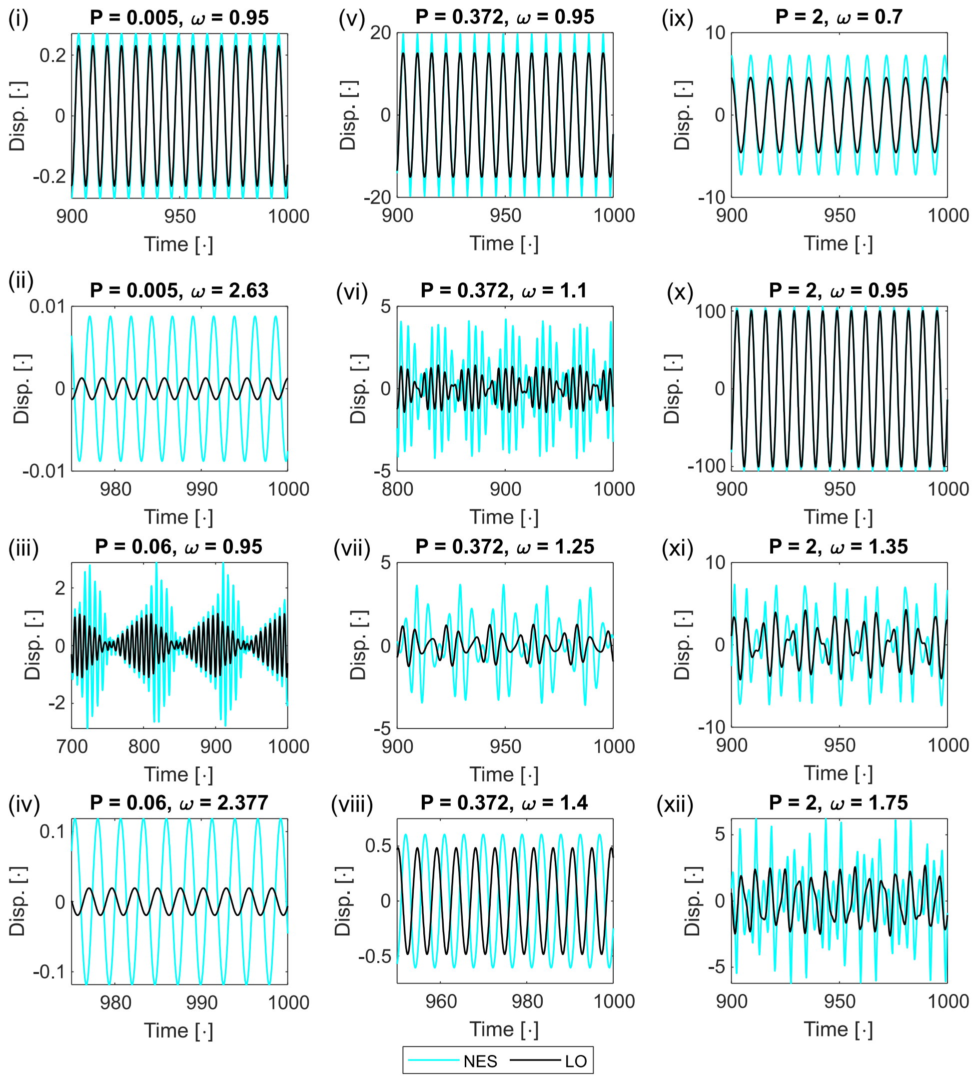

Fig. 8. Simulated response for points i–xii listed on the FRFS depicted on Fig. 7.

dissipated by each damper in the system, which is a common approach to determining the performance of an NES [35–37] second, we compute the 50%, 10%, 5%, and 2% settling times of the LO, which allows us to see how the amplitude of the LO varies across all initial velocities considered.

The energy dissipated by each damper are computed as

$$D_{LO} = \int_0^t \lambda_g \dot{\xi_1}^2 \mathrm{d}t, \tag{9}$$

$$D_{NES} = \int_0^t \lambda_c \left(\dot{\xi}_2 - \dot{\xi}_1\right)^2 \mathrm{d}t. \tag{10}$$

These are normalized by dividing by the initial mechanical energy, $\frac{1}{2}m_1 v_0^2$, then multiplied by 100% to find the percent energy dissipated by each damper. The resulting percent energies dissipated for System I and II are presented in Fig. 9 for all initial velocities considered. At initial velocities at and below 10^{-2}, the behaviors of both systems are identical with the grounding damper dissipating 86% of the total energy and the coupling damper only dissipates 14%. The reason is that, at such low initial velocities, both systems exhibit approximately linear behavior and the response of the system is dominated by motion in the LO. Starting with initial velocities of 10^{-2}, the behavior of System I diverges from that of System II with the amount of energy dissipated by the coupling damper increasing. The amount of energy dissipated by the coupling damper increases gradually initially, then rapidly increases after an initial velocity of ∼0.59 with the two dampers dissipating the same amount of energy at an initial velocity of ∼0.761. The coupling damper dissipates the majority of the energy in the system for the range of initial velocities of [0.761, 6.163], indicating that most of the energy is irreversibly transferred into the NES from the LO inside this range. The two dampers again dissipate equal amounts of energy at an initial velocity of ∼6.163 and, for higher initial velocities, the grounding damper dominates the dissipation of energy. Furthermore, at high initial velocities, the behavior of System I begins to converge to that of System II, which indicates a second regime of linear response at high energies.

Fig. 9 reveals that the LO-NES system coupled by SH spring has two main advantages in energy dissipation over the corresponding cubic nonlinearity LO-NES system: (1) the SH element allows an NES with linear frequency higher than the primary mode to interact with that mode and parasitically absorb energy from it whereas a typical cubic NES is unable to do so; and (2) the use of an SH element results in an increased range where the NES is able to mitigate the motion of the primary structure. The second advantage is due to the softening–hardening behavior (for increasing energy) that arises due to the SH element in the proposed system. Furthermore, we note that the coupling damper in System II never dominates the dissipation of energy in the system, which indicates that the NES is unable to parasitically absorb energy from the LO for any of the initial velocities considered.

To further investigate the performance of the SH and cubic NESs, we also computed the 50%, 10%, 5%, and 2% settling times of the LO for the same simulations performed to compute the percent energy

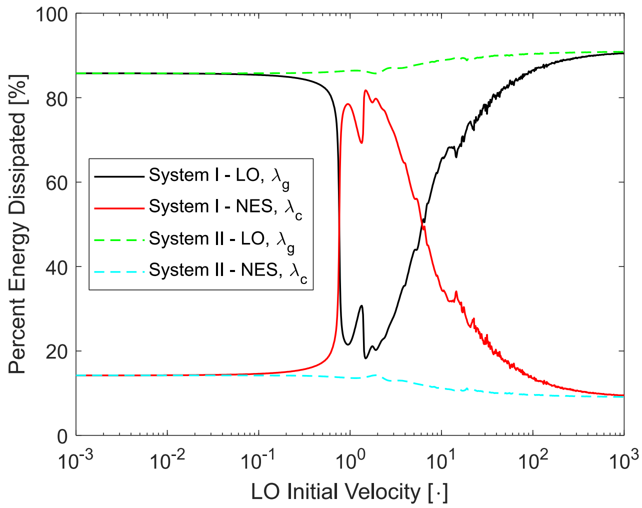

Fig. 9. The percent energy dissipated by each damper for a simulated response time of 3000.

dissipated by each damper as discussed previously [38,39]. The settling times are computed as the final time where the LO achieves 50%, 10%, 5%, and 2% of its maximum displacement amplitude. We chose these four settling percentages to probe how the NES affects the response of the LO in across the entire response window. The resulting plots are presented in Fig. 10 and provide a comparison between the settling times for System I and System II. Similar to Fig. 9, we find that the settling times for both systems agree at low velocities, diverge for a middle range of velocities (roughly 0.1 to 100), then converge to approximately the same time at high initial velocities. The divergence between the two systems arises due to strong decrease in the settling time of the LO in System I, which corresponds to the regime of increased dissipation by the coupling damper. Thus, the reduction of settling times correspond to a irreversible transfer of energy from the first NNM to the second NNM, where the transferred energy becomes trapped and is rapidly dissipated by the NES. Unlike System I, we find that System II has only a minimal effect on the settling time of the LO, which further confirms that the NES in System II is unable to mitigate the motion of the LO.

4. Experimental study and results

4.1. System design and construction

To experimentally assess the performance of an NES with an SH spring, we constructed a physical representation of System I studied in Section 3 and the resulting system is depicted in Fig. 11. The LO consists of a base platform, two mounting blocks for the SH springs, and one mounting block for coupling the NES to the LO using thin steel flexures. The LO base platform is constructed from an aluminum plate of dimensions 0.1524 m × 0.1524 m × 0.0127 m. The LO is grounded to an optical table using two aluminum L-shaped brackets, thin steel flexures, and 10–32 UNF and 1/4″-20 UNC bolts. The steel flexures act as linear grounding springs and are bolted to the L-shaped brackets and the LO base platform using 10–32 UNF bolts. The grounding flexures have dimensions designed as: 0.1143 m×0.1521 m×0.00051 m. Four slotted holes were machined into the LO to allow the mounting blocks for the SH spring to be adjustable to ensure that the SH element contacted the NES without any gaps or precompression. A third mounting block is installed on the LO to provide a point to couple the NES to the LO using two thin steel flexures, which ensures that the NES can be installed the correct height for it to engage the SH strut without issue.

The NES is a cuboid made from steel with dimensions of 0.0305 m × 0.0305 m × 0.0127 m. It is coupled to the third mount on LO linearly using two thin, narrow steel flexures using 6–32 bolts. The portion of these flexures that undergoes bending when the NES moves have dimensions of 0.0584 m × 0.0102 m × 0.000127 m. The NES is nonlinearly coupled to the LO through the SH strut that is mounted onto the LO directly. The mass of completely assembled LO is 0.905 kg and the mass of the NES is 0.095 kg, such that the NES has only 10.5% the mass of the LO.

4.2. Experimental measurements and system identification

In all experiments, we applied an impulsive excitation to the LO directly using a PCB Piezotronics modal hammer (model 086C03) with a black rubber tip installed. We measured the accelerations of the LO and NES using PCB accelerometers (model 352C03) with an average sensitivity of 10 mV/(m/s^2) at a sampling frequency of 4096 Hz for 32 s. The measurements were acquired using a Data Physics Abacus 906 data acquisition system and the Data Physics Software Suite (Data Physics, San Jose, CA, USA). The accelerations were then integrated numerically, and high-pass filtered using a fifth-order Butterworth filter with a cutoff frequency of 4 Hz to obtain the corresponding velocity response. This procedure was then applied to the velocities to obtain the displacement response of both the LO and NES.

To aid in the experimental verification, we first tested the LO without the NES installed and used the resulting data to identify a mathematical model for the LO. In this case, the LO acts as a simple harmonic oscillator governed by the equation of motion

$$m_{LO}\ddot{x} + d_g\dot{x} + k_g x = F(t). \tag{11}$$

We used the resulting response for an impact of 63 N and computed the corresponding FRF for the LO using the integrated displacements. The parameters of the LO were identified using the half-power method, which resulted in $d_g = 1.310$ N s/m ($\zeta = 0.00762$) and $k_g = 8173.3$ N/m ($\omega_n = 95.03$ rad/s, $f_n = 15.125$ Hz). We present a comparison between the FRF computed using the experimental data and the analytical FRF computed using the identified parameters and Eq. (11) in Fig. 12.

Following the identification of the LO, the NES was installed using the thin steel flexures and the SH struts were not installed, such that the resulting system represents a two DOF linear system. In this configuration, an impact was applied directly to the NES using a small PCB modal hammer (model 086E80) and the resulting response was used to identify the stiffness of the thin steel coupling flexures. From these measurements, it was determined that the NES oscillated at a frequency of 2.875 Hz, such that the frequency of the thin steel flexures is approximately 31 N/m (negligible compared to the linear stiffness of the SH strut, which was identified as 4918 N/m in Section 2). Incorporating the linear model for the LO and linear stiffnesses from the SH strut and steel flexures, the resulting natural frequencies of the underlying linear system are $\omega_1 = 14.28$ Hz and $\omega_2 = 38.52$ Hz corresponding to mass-orthonormalized mode shapes of $\phi_1 = [0.982, 1.161]$ and $\phi_2 = [-0.376, 3.030]$. The ratio of the frequency second mode to that of the first mode 2.698:1, which is comparable to the ratio of 2.81:1 found for the theoretical system. The mass-orthonormalized mode shapes of the experimental system also agree well with those of the theoretical system.

After identifying the stiffness of the linear coupling flexures, the SH strut elements were installed, then 15 different impacts ranging from 6 N to 985 N were applied to the LO and the resulting responses were measured using the settings described previously. Since a model for the elastic restoring force SH strut element was identified based on the compression tests discussed in Section 2, the only parameter remaining to be identified is the coefficient of the coupling damper. To this end, we used the responses measured for an impact of 433.5 N to identify the damping coefficient, d_c, using a time series optimization approach used previously in [27,40]. This procedure optimizes the unknown parameters by minimizing the root mean squared error (RMSE) between the experimentally measured and computationally simulated

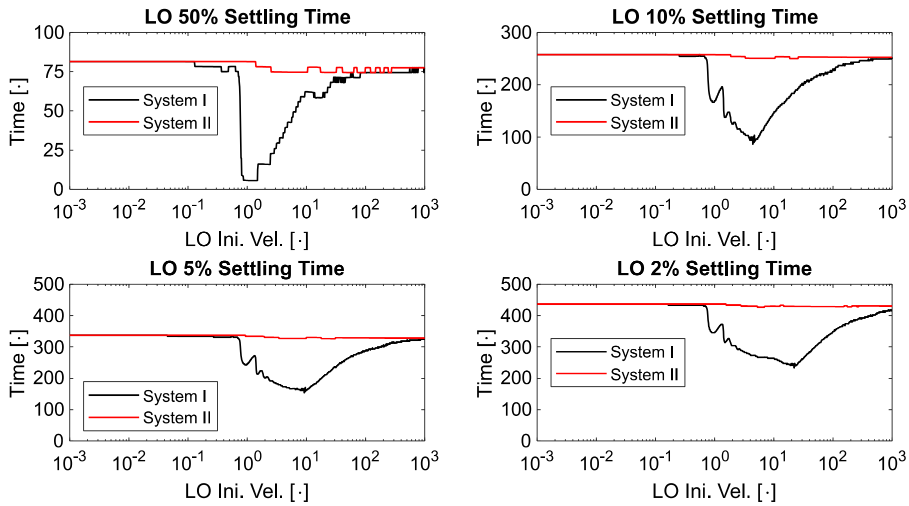

Fig. 10. The 50%, 10%, 5%, and 2% settling times of the LO response for Systems I and II.

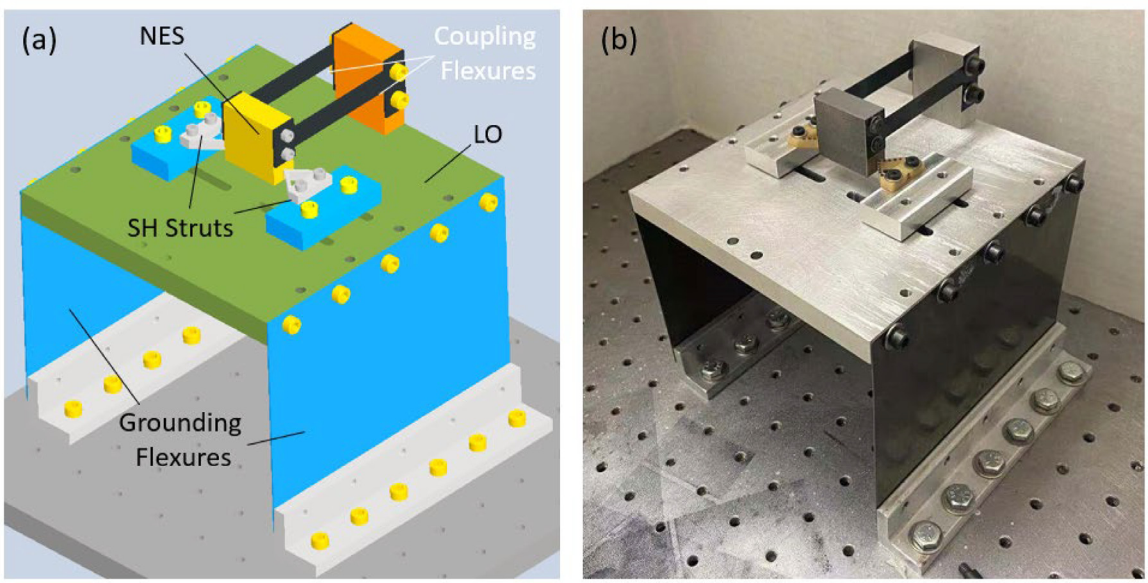

Fig. 11. Setup of the LO-NES system. (a) CAD model, (b) experimental setup.

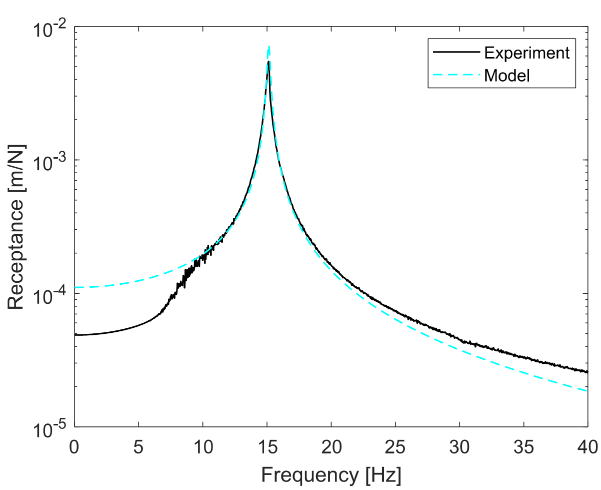

Fig. 12. Comparison of the FRF of the experimentally measured and identified model for the LO without NES installed for an impulsive excitation of 466 N.

responses for both the LO and NES. We implemented this procedure using *patternsearch* in MATLAB®, which is a global optimization method based on direct search, with an initial guess of d_c = 1 N s/m with lower and upper limits of 0 and 5 N s/m, respectively. We used the following settings for the optimization routine: mesh tolerance of 10^{-12}, function tolerance of machine epsilon $\left(2.2204 \times 10^{-16}\right)$, tolerance on variable changes of machine epsilon, maximum function evaluations of 10^{10}, and maximum iterations of 10^{10}. This combination of parameters ensures that the optimization routine stops once the mesh-size drops below 10^{-12} and makes the routine independent of the initial guess, such that it converges to the global minimum. Using this approach, the optimization routine identified that d_c = 2.543 N s/m with the RMSE being 0.00028 and 0.00050 for the LO and NES, respectively. The final physical parameters are provided in Table 5 along with their corresponding non-dimensional values and the non-dimensional values of the theoretical system. We present the resulting comparison between the experimentally measured and computationally simulated responses in Fig. 13(a) and (b) for the LO and NES, respectively. The relative disagreement between the measurement and simulation is due to the simplified model chosen for the SH strut element; however,

Table 5
Parameters of the LO-NES system with dimensional and nondimensional values.

Parameter	Dimensionless values – Theoretical system	Dimensionless values – Experimental system	Dimensional values – Experimental system
m_1	1	1	0.905 kg
m_2	0.1	0.105	0.095 kg
k_g	1	1	8187.7 N/m
k_c	0	0.0038	31 N/m
d_g	0.02	0.0152	1.310 N s/m
d_c	0.02	0.0296	2.543 N s/m
a_1	0.6271	0.6271	4918 N/m
a_2	−1	−1	-4.723×10^6 N/m^2
a_3	0.6494	0.6494	1.847×10^9 N/m^3
a_4	−0.1784	−0.1784	-3.055×10^{11} N/m^4
a_5	0.0184	0.0184	1.903×10^{13} N/m^5

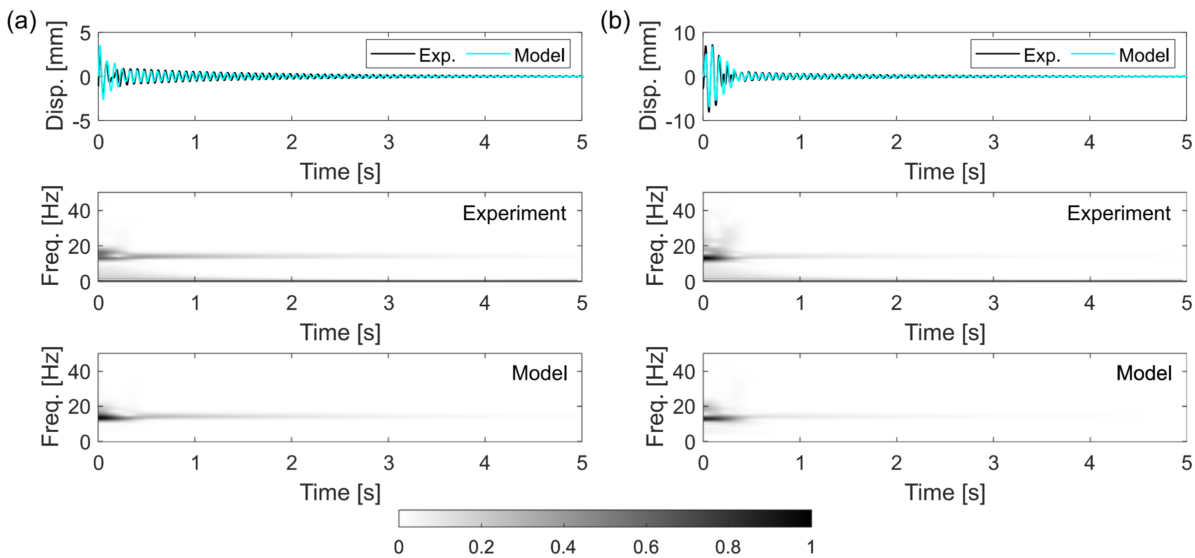

Fig. 13. Comparison between experimental and simulation response of the nonlinear system for an impact of 433.5 N for (a) LO and (b) NES.

the agreement is enough for us to perform predictions regarding the performance of the NES as done in Section 3.

4.3. Experimental verification of proposed NES

To investigate the performance of the experimental SH NES, we simulated the response of the model system under the initial conditions $x_1(0) = x_2(0) = \dot{x}_2(0) = 0$ and $\dot{x}_1(0) = v_0$, such that an initial velocity is applied to only the LO. We simulated the response of the system for 1000 logarithmically spaced initial velocities for the range $v_0 \in \left[10^{-3}, 10^2\right]$ m/s, which provides a large enough range to probe the entire dynamics of the system. The response was simulated using *ode45* in MATLAB® for a time step of 10^{-4} s for a total time of 60 s. Additionally, the relative and absolute tolerances of solver were both set to 10^{-12}. This combination of parameters ensures that the system can be integrated accurately at high initial velocities.

Just as in Section 2, we consider both the percent energy dissipated by each damper and the settling times of the LO. However, unlike the theoretical system, we now provide comparisons between the predictions of the model and the corresponding quantities from the experimental measurements. For the model, the dissipated energies are computed using Eqs. (9) and (10) with $\dot{x}_1$ and $\dot{x}_2$ instead of $\dot{\xi}_1$ and $\dot{\xi}_2$ and the dimensional values for each parameter. The resulting values are normalized by the initial mechanical energy, $\frac{1}{2}m_1 v_0^2$, then multiplied by 100 to obtain the percent energy dissipated by each damper. For the experiments, the dissipated energies are computed using Eqs. (9) and (10) using the measured velocities and the dimensional parameters. However, the maximum mechanical energy is unknown in the experiments, since the excitation is due to an impulse supplied by a

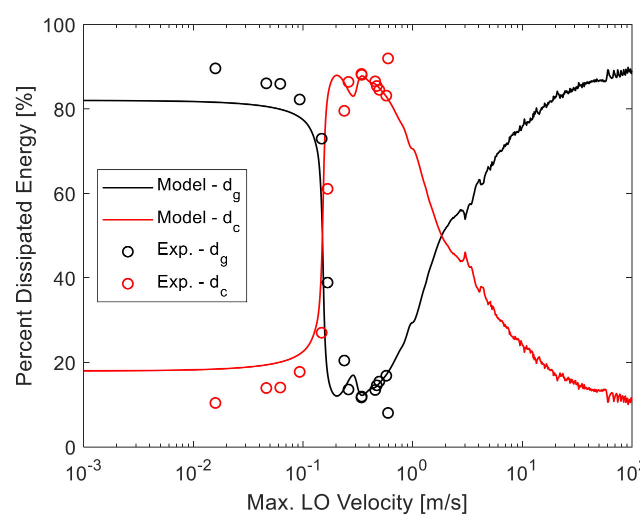

Fig. 14. The percent energy dissipated by each damper for both the dimensional model and the experimental measurements.

modal impact hammer. Thus, we normalize the dissipated energies by their sum and multiply the result by 100 to obtain the percent energy dissipated for each damper. The procedure applied to the experiments can also be applied to the simulation results, but the outcome is the same as normalizing by the initial mechanical energy. We depict the percent energy dissipated by each damper as functions of the maximum

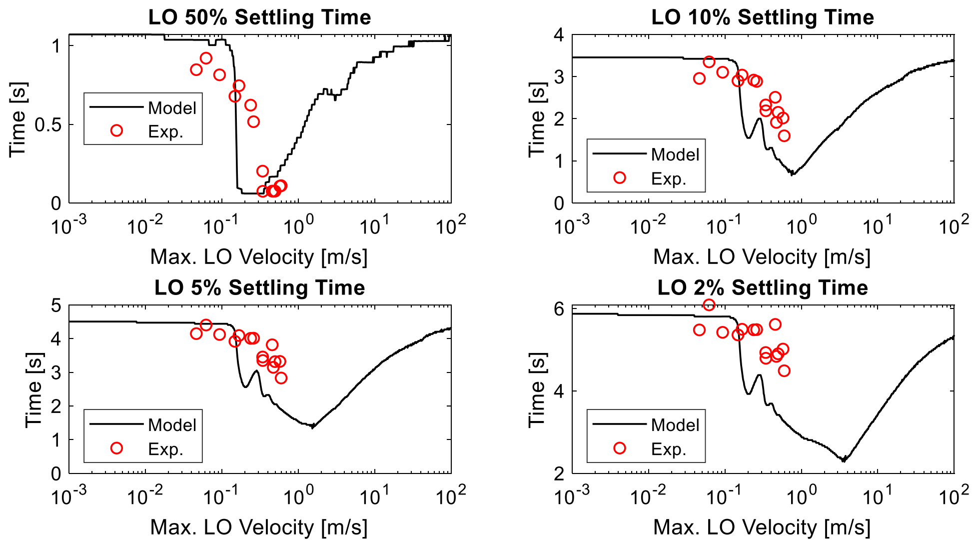

Fig. 15. The percent energy dissipated by each damper for both the dimensional model and the experimental measurements.

absolute velocity of the LO (i.e. the initial velocity in the case of the model) in Fig. 14. A good agreement is observed between the experimental and model results, which confirms the accuracy of the theoretical predictions. Although we were able to force the system with impacts higher than 1000 N, we found that the NES would jump out of its stable position between the two SH elements, resulting in a bifurcation that drastically changes the dynamics of the system. Thus, we excluded any forces where this occurred and were unable to achieve maximum LO velocities above 1 m/s.

As a second verification of the performance of the experimental NES, we computed the 50%, 10%, 5%, and 2% settling times for both the model and the experimental measurements. We depict the resulting comparison in Fig. 15. Although there is some minor disagreement between the predicted and measured settling times, there is good agreement in the trends of the two data sets. The agreement in trends confirms the accuracy of the theoretical results and the ability of an NES with an SH element to mitigate vibrations that occur at frequencies below its own linear (low energy) frequency.

5. Concluding remarks

This research focused on the mitigation of vibrations using a NES that had a linear, low-energy frequency above those vibrations using an SH strut element, which had a restoring force consisting of a linear segment, a plateau, and a stiffening segment. This combination of regimes caused the NES to undergo softening then hardening for increasing displacements, which gives it the ability to interact with vibrations occurring below its linear, low-energy frequency. The performance of the SH NES was compared with the performance of an NES with the same linear stiffness as the SH NES but with only a cubic nonlinear stiffness term. The comparison showed that the cubic NES was unable to interact with the LO whereas the SH NES was able to mitigate the motion of the LO within a certain regime of initial velocities. The theoretical results for the SH NES were validated experimentally with a comparable dimensional system. The results of this research demonstrate that SH elements can be incorporated into NESs to allow them to interact with vibrations that occur below their own linear, low-energy frequencies. Such NESs could find use in highly flexible structures with very low natural frequencies where conventional NESs or tuned-mass-dampers are unable to mitigate the vibrations. Furthermore, because the SH NES undergoes two regimes of nonlinear behavior (softening and hardening), it may improve upon the range of effectiveness of standard NESs allowing them to mitigate motion across wider ranges of excitation.

CRediT authorship contribution statement

Chengen Wang: Conceptualization, Methodology, Formal analysis, Software, Data curation, Investigation, Validation, Writing – original draft, Writing – review & editing, Visualization. **Ethan J. Krings:** Methodology, Investigation, Resources, Writing – review & editing. **Anna T. Allen:** Conceptualization, Methodology, Formal analysis, Software, Writing – original draft. **Eric J. Markvicka:** Resources, Writing – review & editing, Supervision, Project administration, Funding acquisition. **Keegan J. Moore:** Software, Validation, Formal analysis, Writing – original draft, Writing – review & editing, Supervision, Resources, Funding acquisition, Project administration.

Declaration of competing interest

The authors declare that they have no known competing financial interests or personal relationships that could have appeared to influence the work reported in this paper.

Acknowledgments

EJK and EJM acknowledge support through the Nebraska Tobacco Settlement Biomedical Research Development Fund. KJM and CW acknowledge support through Nebraska EPSCoR FIRST grant number OIA-1557417.

Appendix A. Supplementary data

Supplementary material related to this article can be found online at https://doi.org/10.1016/j.ijnonlinmec.2022.104194.

References

[1] G. Kerschen, M. Peeters, J.C. Golinval, A.F. Vakakis, Nonlinear normal modes, Part I: A useful framework for the structural dynamicist, Mech. Syst. Signal Process. 23 (1) (2009) 170–194, http://dx.doi.org/10.1016/j.ymssp.2008.04.002.
[2] M. Peeters, R. Viguié, G. Sérandour, G. Kerschen, J.-C. Golinval, Nonlinear normal modes, Part II: Toward a practical computation using numerical continuation techniques, Mech. Syst. Signal Process. 23 (1) (2009) 195–216, http://dx.doi.org/10.1016/j.ymssp.2008.04.003.
[3] A.F. Vakakis, O.V. Gendelman, L.A. Bergman, D.M. McFarland, G. Kerschen, Y.S. Lee, Nonlinear Targeted Energy Transfer in Mechanical and Structural Systems. Vol. 156, Sprinnger Netherlands, 2008.
[4] Y. Zhang, K.J. Moore, D.M. McFarland, A.F. Vakakis, Targeted energy transfers and passive acoustic wave redirection in a two-dimensional granular network under periodic excitation, J. Appl. Phys. 118 (23) (2015) 234901.

[5] A. Luongo, D. Zulli, Dynamic analysis of externally excited NES-controlled systems via a mixed multiple scale/harmonic balance algorithm, Nonlinear Dynam. 70 (3) (2012) 2049–2061, http://dx.doi.org/10.1007/s11071-012-0597-6.

[6] Z.-W. Fang, Y.-W. Zhang, X. Li, H. Ding, L.-Q. Chen, Complexification-averaging analysis on a giant magnetostrictive harvester integrated with a nonlinear energy sink, J. Vib. Acoust. 140 (2) (2018) 021009, http://dx.doi.org/10.1115/1.4038033.

[7] Y. Starosvetsky, O.V. Gendelman, Bifurcations of attractors in forced system with nonlinear energy sink: the effect of mass asymmetry, Nonlinear Dynam. 59 (4) (2010) 711–731, http://dx.doi.org/10.1007/s11071-009-9572-2.

[8] A.H. Nayfeh, D.T. Mook, Nonlinear Oscillations, in: Wilty Classics Library, John Wiley & Sons, 2008.

[9] K.J. Moore, M. Kurt, M. Eriten, D.M. McFarland, L.A. Bergman, A.F. Vakakis, Time-series-based nonlinear system identification of strongly nonlinear attachments, J. Sound Vib. 438 (2019) 13–32, http://dx.doi.org/10.1016/j.jsv.2018.09.033.

[10] Y. Chai, X. Jing, X. Chao, X-shaped mechanism based enhanced tunable QZS property for passive vibration isolation, Int. J. Mech. Sci. 218 (2022) 107077, http://dx.doi.org/10.1016/j.ijmecsci.2022.107077.

[11] A. Carrella, M.J. Brennan, T.P. Waters, V. Lopes, Force and displacement transmissibility of a nonlinear isolator with high-static-low-dynamic-stiffness, Int. J. Mech. Sci. 55 (1) (2012) 22–29, http://dx.doi.org/10.1016/j.ijmecsci.2011.11.012.

[12] A. Carrella, M.J. Brennan, T.P. Waters, Static analysis of a passive vibration isolator with quasi-zero-stiffness characteristic, J. Sound Vib. 301 (3–5) (2007) 678–689, http://dx.doi.org/10.1016/j.jsv.2006.10.011.

[13] S. Weizhi, L. Zhien, L. Chihua, L. Bin, Z. Derong, N. Fuqua, Analysis of vibration suppression performance of nonlinear energy sink with negative stiffness, J. Vib. Eng. Technol. (2022) http://dx.doi.org/10.1007/s42417-022-00462-7.

[14] J. Zhou, D. Xu, S. Bishop, A torsion quasi-zero stiffness vibration isolator, J. Sound Vib. 338 (2015) 121–133, http://dx.doi.org/10.1016/j.jsv.2014.10.027.

[15] J. Zhou, X. Wang, D. Xu, S. Bishop, Nonlinear dynamic characteristics of a quasi-zero stiffness vibration isolator with cam–roller–spring mechanisms, J. Sound Vib. 346 (2015) 53–69, http://dx.doi.org/10.1016/j.jsv.2015.02.005.

[16] K. Ye, J.C. Ji, T. Brown, Design of a quasi-zero stiffness isolation system for supporting different loads, J. Sound Vib. 471 (2020) 115198, http://dx.doi.org/10.1016/j.jsv.2020.115198.

[17] X. Liu, X. Huang, H. Hua, On the characteristics of a quasi-zero stiffness isolator using Euler buckled beam as negative stiffness corrector, J. Sound Vib. 332 (14) (2013) 3359–3376, http://dx.doi.org/10.1016/j.jsv.2012.10.037.

[18] H. Ding, L.-Q. Chen, Nonlinear vibration of a slightly curved beam with quasi-zero-stiffness isolators, Nonlinear Dynam. 95 (3) (2019) 2367–2382, http://dx.doi.org/10.1007/s11071-018-4697-9.

[19] X. Liu, Q. Zhao, Z. Zhang, X. Zhou, An experiment investigation on the effect of Coulomb friction on the displacement transmissibility of a quasi-zero stiffness isolator, J. Mech. Sci. Technol. 33 (1) (2019) 121–127, http://dx.doi.org/10.1007/s12206-018-1212-7.

[20] Y. Zeng, H. Ding, R.-H. Du, L.-Q. Chen, Micro-amplitude vibration suppression of a bistable nonlinear energy sink constructed by a buckling beam, Nonlinear Dynam. (2022) http://dx.doi.org/10.1007/s11071-022-07378-7.

[21] W.S. Robertson, M.R.F. Kidner, B.S. Cazzolato, A.C. Zander, Theoretical design parameters for a quasi-zero stiffness magnetic spring for vibration isolation, J. Sound Vib. 326 (1–2) (2009) 88–103, http://dx.doi.org/10.1016/j.jsv.2009.04.015.

[22] V. Klitnoi, A. Gaydamaka, On the problem of vibration protection of rotor systems with elastic adaptive elements of quasi-zero stiffness, Diagnostyka 21 (2) (2020) 69–75, http://dx.doi.org/10.29354/diag/122533.

[23] K. Wang, J. Zhou, H. Ouyang, Y. Chang, D. Xu, A dual quasi-zero-stiffness sliding-mode triboelectric nanogenerator for harvesting ultralow-low frequency vibration energy, Mech. Syst. Signal Process. 151 (2021) 107368, http://dx.doi.org/10.1016/j.ymssp.2020.107368.

[24] C. Cai, J. Zhou, L. Wu, K. Wang, D. Xu, H. Ouyang, Design and numerical validation of quasi-zero-stiffness metamaterials for very low-frequency band gaps, Compos. Struct. 236 (2020) 111862, http://dx.doi.org/10.1016/j.compstruct.2020.111862.

[25] K. Wang, J. Zhou, H. Ouyang, L. Cheng, D. Xu, A semi-active metamaterial beam with electromagnetic quasi-zero-stiffness resonators for ultralow-frequency band gap tuning, Int. J. Mech. Sci. 176 (2020) 105548, http://dx.doi.org/10.1016/j.ijmecsci.2020.105548.

[26] J. Bunyan, S. Tawfick, Exploiting structural instability to design architected materials having essentially nonlinear stiffness, Adv. Energy Mater. 21 (2) (2019) 1800791, http://dx.doi.org/10.1002/adem.201800791.

[27] C. Wang, K.J. Moore, On nonlinear energy flows in nonlinearly coupled oscillators with equal mass, Nonlinear Dynam. 103 (1) (2021) 343–366, http://dx.doi.org/10.1007/s11071-020-06120-5.

[28] A. Singh, K.J. Moore, Characteristic nonlinear system identification of local attachments with clearance nonlinearities, Nonlinear Dynam. 102 (3) (2020) 1667–1684.

[29] C. Berthold, J. Gross, C. Frey, M. Krack, Development of a fully-coupled harmonic balance method and a refined energy method for the computation of flutter-induced Limit Cycle Oscillations of bladed disks with nonlinear friction contacts, J. Fluids Struct. 102 (2021) 103233, http://dx.doi.org/10.1016/j.jfluidstructs.2021.103233.

[30] L. Chen, B. Basu, S.R.K. Nielsen, Nonlinear periodic response analysis of mooring cables using harmonic balance method, J. Sound Vib. 438 (2019) 402–418, http://dx.doi.org/10.1016/j.jsv.2018.09.027.

[31] S. Wang, L. Hua, C. Yang, Y. Zhang, X. Tan, Nonlinear vibrations of a piecewise-linear quarter-car truck model by incremental harmonic balance method, Nonlinear Dynam. 92 (4) (2018) 1719–1732, http://dx.doi.org/10.1007/s11071-018-4157-6.

[32] L.-S. Wei, Y.-Z. Wang, Y.-S. Wang, Nonreciprocal transmission of nonlinear elastic wave metamaterials by incremental harmonic balance method, Int. J. Mech. Sci. 173 (2020) 105433, http://dx.doi.org/10.1016/j.ijmecsci.2020.105433.

[33] B. Kaviya, R. Suresh, V.K. Chandrasekar, B. Balachandran, Influence of dissipation on extreme oscillations of a forced anharmonic oscillator, Int. J. Non-Linear Mech. 127 (2020) 103596, http://dx.doi.org/10.1016/j.ijnonlinmec.2020.103596.

[34] Y. Chen, B. Zhang, N. Zhang, M. Zheng, A condensation method for the dynamic analysis of vertical vehicle–track interaction considering vehicle flexibility, J. Vib. Acoust. 137 (4) (2015) 041010, http://dx.doi.org/10.1115/1.4029947.

[35] A.F. Vakakis, Passive nonlinear targeted energy transfer, Phil. Trans. R. Soc. A 376 (2127) (2018) 20170132, http://dx.doi.org/10.1098/rsta.2017.0132.

[36] A.F. Vakakis, O.V. Gendelman, L.A. Bergman, A. Mojahed, M. Gzal, Nonlinear targeted energy transfer: state of the art and new perspectives, Nonlinear Dynam. (2022) http://dx.doi.org/10.1007/s11071-022-07216-w.

[37] J.E. Chen, W. He, W. Zhang, M.H. Yao, J. Liu, M. Sun, Vibration suppression and higher branch responses of beam with parallel nonlinear energy sinks, Nonlinear Dynam. 91 (2) (2018) 885–904, http://dx.doi.org/10.1007/s11071-017-3917-z.

[38] A. Khassetarash, R. Hassannejad, M.M. Ettefagh, A.E. Oskouei, Vibration settling time of the gastrocnemius remains constant during an exhaustive run in rear foot strike runners, J. Biomech. 93 (2019) 140–146, http://dx.doi.org/10.1016/j.jbiomech.2019.06.026.

[39] S. Zhang, X. He, Q. Chen, Energy coupled–dissipation control for 3-dimensional overhead cranes, Nonlinear Dynam. 99 (3) (2020) 2097–2107, http://dx.doi.org/10.1007/s11071-019-05451-2.

[40] K.J. Moore, J. Bunyan, S. Tawfick, O.V. Gendelman, S. Li, M. Leamy, A.F. Vakakis, Nonreciprocity in the dynamics of coupled oscillators with nonlinearity, asymmetry, and scale hierarchy, Phys. Rev. E 97 (1) (2018) 012219, http://dx.doi.org/10.1103/PhysRevE.97.012219.